

Multivariate Variational Autoencoder

Mehmet Can Yavuz

Faculty of Engineering and Natural Sciences

Işık University, İstanbul, Türkiye

mehmetcan.yavuz@isikun.edu.tr

Abstract—We present the Multivariate Variational Autoencoder (MVAE), a VAE variant that preserves Gaussian tractability while lifting the diagonal posterior restriction. MVAE factorizes each posterior covariance, where a *global coupling matrix* \mathbf{C} induces dataset-wide latent correlations and *per-sample diagonal scales* modulate local uncertainty. This yields a full-covariance family with analytic KL and an efficient reparameterization via $\mathbf{L} = \mathbf{C}\text{diag}(\boldsymbol{\sigma})$. Across Larochelle-style MNIST variants, Fashion-MNIST, CIFAR-10, and CIFAR-100, MVAE consistently matches or improves reconstruction (MSE \downarrow) and delivers robust gains in calibration (NLL/Brier/ECE \downarrow) and unsupervised structure (NMI/ARI \uparrow) relative to diagonal-covariance VAEs with matched capacity, especially at mid-range latent sizes. Latent-plane visualizations further indicate smoother, more coherent factor traversals and sharper local detail. We release a fully reproducible implementation with training/evaluation scripts and sweep utilities to facilitate fair comparison and reuse.

Index Terms—Multivariate, Variational Autoencoder, Full-Covariance Posterior, Latent Correlation Modeling, Representation Learning

I. INTRODUCTION

Learning compact yet expressive latent representations that support both high-fidelity generation and downstream discrimination remains a central objective in modern machine learning. Variational Autoencoders (VAEs) [1], [2] address this goal by maximizing an evidence lower bound (ELBO) that jointly encourages accurate reconstructions and a regularized approximate posterior over latent variables. However, the conventional VAE parameterizes the encoder posterior with a *diagonal* covariance, implicitly assuming conditional independence among latent coordinates. This factorization simplifies optimization but constrains the geometry of the latent manifold, often producing entangled or redundant dimensions and exacerbating posterior collapse in high-capacity decoders.

We address these limitations with a *Multivariate Variational Autoencoder (MVAE)* that augments the encoder with (i) a *sample-specific* diagonal scale and (ii) a *global coupling matrix* that induces persistent correlations in the latent space. Formally, each posterior is expressed as

$$q_{\phi}(\mathbf{z} \mid \mathbf{x}) = \mathcal{N}(\boldsymbol{\mu}_{\phi}(\mathbf{x}), \mathbf{C} \text{diag}(\boldsymbol{\sigma}_{\phi}^2(\mathbf{x})) \mathbf{C}^{\top}),$$

where the learnable matrix \mathbf{C} captures dataset-level dependencies while $\boldsymbol{\sigma}_{\phi}(\mathbf{x})$ modulates per-sample uncertainty. This decomposition yields a structured full-covariance family with analytic KL divergence, maintaining computational tractability while substantially enriching posterior geometry. In addition, the mean is linearly coupled through \mathbf{C} , enabling anisotropic yet interpretable transformations across latent dimensions.

Empirically, across Larochelle-style MNIST variants [3], [4], Fashion-MNIST [5], and CIFAR-10/100 [6], MVAE consistently improves over diagonal-covariance VAEs of matched capacity in terms of ELBO (\uparrow), reconstruction error (\downarrow), calibration quality (NLL, Brier, ECE; \downarrow), and unsupervised structure (NMI/ARI; \uparrow). These gains confirm that incorporating correlated uncertainty and mean coupling leads to more robust and informative latent spaces.

Beyond generative quality, we explicitly evaluate the *usefulness* of learned representations through linear probing, clustering, and probabilistic calibration. Together, these complementary criteria—generation, discrimination, calibration, and structure—provide a holistic view of latent-space quality that better reflects practical deployment. To facilitate reproducibility, we release complete training and evaluation pipelines, including metrics, dataset splits, and sweep utilities.

Contributions. (1) We propose the Multivariate Variational Autoencoder (MVAE), which integrates a global coupling matrix and per-sample scales to realize a full-covariance Gaussian posterior with closed-form KL divergence. (2) We introduce a principled, multi-criterion evaluation framework combining ELBO, reconstruction fidelity, linear probing, calibration, and clustering under standardized seeds and data splits. (3) We release an open, fully reproducible implementation with scripts, logs, and evaluation utilities to enable fair and transparent comparisons.

II. RELATED WORK

a) VAEs and posterior expressiveness.: The Variational Autoencoder (VAE) framework [1], [2] popularized amortized variational inference via the reparameterization trick, typically under a diagonal Gaussian posterior. Subsequent research has sought to enhance posterior flexibility while retaining tractable objectives. Normalizing flows transform simple posteriors into richer distributions through invertible mappings [7], [8], while auxiliary-variable and hierarchical extensions further expand expressiveness [9], [10]. Mixture-based or learned prior formulations such as VampPrior [11] enrich the generative model by increasing prior diversity. Our approach is orthogonal and complementary: we retain a Gaussian posterior but remove the diagonal restriction by learning a full covariance.

b) Full-covariance variational families.: Full-covariance posteriors in deep VAEs have been explored through structured covariance parameterizations—e.g., low-rank plus diagonal decompositions, precision (information) parameterizations, or

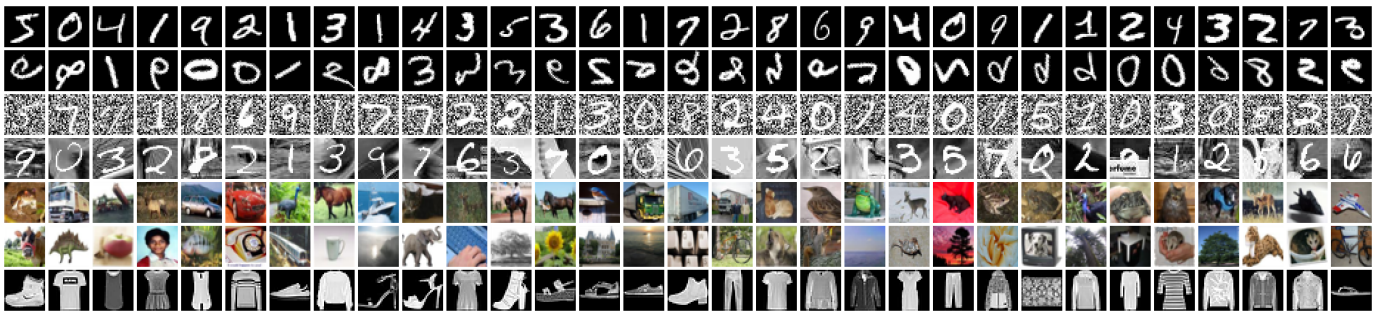


Fig. 1: Representative samples from all benchmark datasets employed in our study. Each row (from top to bottom) corresponds to MNIST Basic, MNIST Rotated, MNIST with Random Backgrounds, MNIST with Background Images, CIFAR-10, CIFAR-100, and Fashion-MNIST. These examples illustrate the diversity in visual complexity, background texture, and object categories across datasets.

Kronecker/sparse structures—to balance flexibility and computational cost [12], [13]. The proposed coupling-matrix formulation falls within this line of work, but emphasizes a global, data-shared correlation structure that remains amortized and lightweight.

c) Disentanglement, structure, and robustness.:

Disentanglement-oriented VAEs, such as β -VAE [14], FactorVAE [15], and β -TCVAE [16], promote statistically independent latent factors but often trade off reconstruction fidelity and are sensitive to hyperparameter tuning. In contrast, our coupling matrix introduces *controlled anisotropy* in the latent mean, improving linear separability and clustering without relying on mutual-information surrogates or adversarial penalties. Complementary robustness analyses—particularly those using Larochelle-style MNIST variants with structured and unstructured corruptions [3], [4]—suggest that correlated posteriors generalize better under geometric and background perturbations.

d) Evaluation beyond likelihood.:

ELBO or likelihood-based metrics alone may not fully reflect representation quality. Linear probes [17], clustering indices, and calibration metrics [18], [19] provide complementary perspectives on separability, structure, and uncertainty reliability. Accordingly, we report a unified set of (\uparrow/\downarrow)-oriented metrics—ELBO, per-pixel MSE, probe accuracy/NLL/Brier/ECE, and NMI/ARI—to provide a more faithful and multidimensional evaluation of model quality under consistent capacity and training budgets.

e) Positioning.:

Compared to flow-augmented VAEs [7], [8], our Multivariate VAE (MVAE) maintains a simple and computationally efficient encoder–decoder architecture while explicitly modeling latent correlations through a global coupling matrix. Relative to disentanglement-penalized approaches [14]–[16], we rely on geometric structure rather than additional regularization terms. These choices yield consistent performance gains across diverse visual domains (digits, fashion, and natural images) with minimal engineering overhead and seamless integration into existing VAE pipelines.

III. DATASETS

To evaluate the robustness and generalization capacity of our proposed method, we conducted experiments on a diverse suite of classification datasets that differ in background composition, rotation, visual complexity, and synthetic constraints. The datasets are derived from canonical benchmarks introduced by Larochelle *et al.* [3] and Vincent *et al.* [4], with most being extensions or variants of the MNIST handwritten digit dataset [20]. Each dataset is briefly summarized below with details on its structure, preprocessing, and data splits. All datasets and accompanying code are publicly available.¹²

- **MNIST Basic:** This dataset consists of 28×28 grayscale images of handwritten digits (0–9), each belonging to one of ten classes. To ensure balanced training and consistent model comparison, we reorganized the original MNIST splits into 10,000 training, 2,000 validation, and 50,000 test samples. The images feature white digits on a black background, with pixel intensities normalized to the $[0, 1]$ range.
- **MNIST with Background Images:** A modified version of MNIST Basic in which digits are overlaid on 28×28 natural image patches. The combination is performed by taking the pixel-wise maximum between the digit and the background patch. Low-variance patches are excluded to maintain visual diversity. The dataset retains the same class labels and data splits as MNIST Basic.
- **MNIST with Random Backgrounds:** This variant overlays the white foreground digits on random noise backgrounds generated by uniformly sampling pixel values from $(0, 1)$. It follows the same data structure and split sizes as MNIST Basic, with ten digit classes and identical training, validation, and test partitions.
- **Rotated MNIST:** In this dataset, each MNIST digit is randomly rotated by an angle uniformly drawn from $[0, 2\pi)$. The dataset preserves the ten-class structure and consists of 10,000 training, 2,000 validation, and 50,000

¹HuggingFace Dataset

²GitHub Repository

test examples. This configuration tests the model’s ability to learn rotation-invariant representations.

- **CIFAR-10:** The CIFAR-10 dataset contains 60,000 color images of size 32×32 across ten object categories (*airplane, automobile, bird, cat, deer, dog, frog, horse, ship, truck*). Following the standard split, there are 50,000 training and 10,000 test images, with 5,000 training samples held out for validation. Each class contributes an equal number of examples.
- **CIFAR-100:** An extension of CIFAR-10, this dataset includes 100 fine-grained object classes organized hierarchically into 20 superclasses. It comprises 60,000 color images of size 32×32 , with each class containing 600 examples. The standard split includes 50,000 training and 10,000 test samples, and 5,000 training images are reserved for validation during model selection.
- **Fashion-MNIST:** Designed as a more challenging alternative to MNIST, Fashion-MNIST contains 28×28 grayscale images of clothing items spanning ten categories (*T-shirt/top, trouser, pullover, dress, coat, sandal, shirt, sneaker, bag, ankle boot*). It provides 60,000 training and 10,000 test images, with 10,000 training samples set aside for validation.

Collectively, these datasets encompass a wide range of variations in texture, orientation, and background complexity, enabling comprehensive evaluation of the proposed method’s resilience to both structured and unstructured perturbations. Representative examples are visualized in Fig. 1.

IV. METHODOLOGY

A. Variational Autoencoder

Variational Autoencoders (VAEs) learn a low-dimensional latent representation $\mathbf{z} \in \mathbb{R}^{d_z}$ of a high-dimensional observation $\mathbf{x} \in \mathbb{R}^D$. A VAE posits an encoder (approximate posterior) $q_\phi(\mathbf{z} | \mathbf{x})$ and a decoder (likelihood) $p_\theta(\mathbf{x} | \mathbf{z})$, with a standard normal prior $p(\mathbf{z}) = \mathcal{N}(\mathbf{0}, \mathbf{I})$. The learning objective is to *maximize* the evidence lower bound (ELBO):

$$\mathcal{L}(\theta, \phi; \mathbf{x}) = \mathbb{E}_{q_\phi(\mathbf{z}|\mathbf{x})}[\log p_\theta(\mathbf{x} | \mathbf{z})] - D_{\text{KL}}(q_\phi(\mathbf{z} | \mathbf{x}) \| p(\mathbf{z})), \quad (1)$$

which balances reconstruction fidelity (first term) against a regularizer that encourages the posterior to remain close to the prior (second term).

B. Diagonal Covariance Limitation

In conventional VAEs, the encoder outputs a mean vector $\boldsymbol{\mu}_\phi(\mathbf{x})$ and a log-variance vector $\log \boldsymbol{\sigma}_\phi^2(\mathbf{x})$, yielding a factorized posterior

$$q_\phi(\mathbf{z} | \mathbf{x}) = \mathcal{N}(\boldsymbol{\mu}_\phi(\mathbf{x}), \text{diag}(\boldsymbol{\sigma}_\phi^2(\mathbf{x}))). \quad (2)$$

While computationally attractive, this independence assumption prevents the posterior from capturing cross-dimensional correlations in \mathbf{z} , often leading to *redundant* or *entangled* coordinates that encode overlapping information [21].

C. Full-Covariance Variational Formulation

To overcome this limitation, we adopt a full-covariance Gaussian posterior:

$$q_\phi(\mathbf{z} | \mathbf{x}) = \mathcal{N}(\boldsymbol{\mu}_\phi(\mathbf{x}), \boldsymbol{\Sigma}_\phi(\mathbf{x})), \quad (3)$$

with $\boldsymbol{\Sigma}_\phi(\mathbf{x}) \in \mathbb{R}^{d_z \times d_z}$ symmetric positive (semi-)definite. Naively parameterizing $\boldsymbol{\Sigma}_\phi(\mathbf{x})$ is prohibitive ($O(d_z^2)$ per sample) and must enforce positive-definiteness. We therefore decompose $\boldsymbol{\Sigma}_\phi(\mathbf{x})$ into a structured form that combines a *global* coupling matrix with *sample-specific* diagonal scales.

D. Coupling-Matrix Posterior

Let $\mathbf{C} \in \mathbb{R}^{d_z \times d_z}$ be a dataset-wide, learnable coupling matrix that induces persistent latent correlations. For each \mathbf{x} , the encoder outputs $\boldsymbol{\mu}_\phi(\mathbf{x})$ and a diagonal scale vector $\boldsymbol{\sigma}_\phi(\mathbf{x}) > 0$, and we set

$$\boldsymbol{\Sigma}_\phi(\mathbf{x}) = \mathbf{C} \text{diag}(\boldsymbol{\sigma}_\phi^2(\mathbf{x})) \mathbf{C}^\top. \quad (4)$$

Equivalently, define the per-sample factor $\mathbf{L}_\phi(\mathbf{x}) = \mathbf{C} \text{diag}(\boldsymbol{\sigma}_\phi(\mathbf{x}))$ so that $\boldsymbol{\Sigma}_\phi(\mathbf{x}) = \mathbf{L}_\phi(\mathbf{x}) \mathbf{L}_\phi(\mathbf{x})^\top$. The reparameterization becomes

$$\mathbf{z} = \boldsymbol{\mu}_\phi(\mathbf{x}) + \mathbf{L}_\phi(\mathbf{x}) \boldsymbol{\epsilon}, \quad \boldsymbol{\epsilon} \sim \mathcal{N}(\mathbf{0}, \mathbf{I}), \quad (5)$$

which is differentiable w.r.t. both ϕ and \mathbf{C} . Intuitively, \mathbf{C} captures dataset-level rotations/correlations in the latent space, while the per-sample scales modulate local uncertainty.

E. Closed-Form KL Divergence

With the standard normal prior, the KL divergence remains analytic:

$$D_{\text{KL}}(q_\phi(\mathbf{z} | \mathbf{x}) \| p(\mathbf{z})) = \frac{1}{2} \left[\text{tr}(\boldsymbol{\Sigma}_\phi(\mathbf{x})) + \|\boldsymbol{\mu}_\phi(\mathbf{x})\|_2^2 - d_z - \log \det \boldsymbol{\Sigma}_\phi(\mathbf{x}) \right]. \quad (6)$$

Using $\boldsymbol{\Sigma}_\phi = \mathbf{L} \mathbf{L}^\top$ with $\mathbf{L} = \mathbf{C} \text{diag}(\boldsymbol{\sigma}_\phi)$, we have $\log \det \boldsymbol{\Sigma}_\phi = 2 \log |\det \mathbf{L}|$.

F. Training Objective

We minimize the negative ELBO over the dataset:

$$\mathcal{J}_{\text{MVAE}}(\theta, \phi) = \frac{1}{N} \sum_{n=1}^N (-\mathbb{E}_{q_\phi(\mathbf{z}|\mathbf{x}_n)}[\log p_\theta(\mathbf{x}_n | \mathbf{z})] + D_{\text{KL}}(q_\phi(\mathbf{z} | \mathbf{x}_n) \| p(\mathbf{z}))). \quad (7)$$

For Bernoulli likelihoods we use the binary cross-entropy; for Gaussian likelihoods we use the Gaussian negative log-likelihood (which reduces to MSE if the observation variance is fixed). The parameter cost of \mathbf{C} scales as $O(d_z^2)$ but is amortized across samples, while per-sample costs remain linear in d_z thanks to diagonal scales.

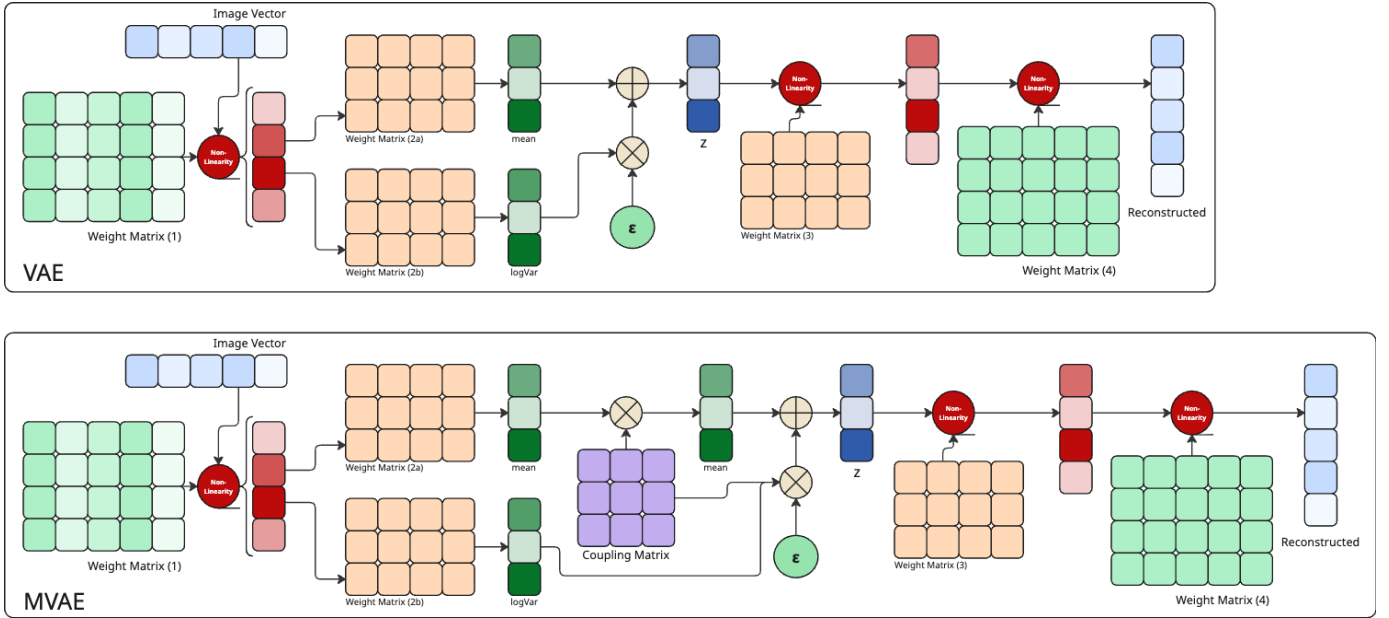


Fig. 2: Comparison of the standard VAE and the proposed MVAE. The VAE (top) encodes inputs into a mean and diagonal log-variance, assuming independent latent dimensions. The MVAE (bottom) augments this with a coupling matrix that induces correlated latent variables via a full covariance $q(\mathbf{z}|\mathbf{x})$, capturing structured dependencies for richer representations.

V. EXPERIMENTAL RESULTS

A. Experimental Setup

Each configuration was defined by a dataset–model–latent-size triplet, ensuring a systematic exploration of both the baseline and proposed architectures. For every dataset, we trained models with latent dimensions ranging from low to high capacity (typically $d_z \in \{2, 4, 16, 32, 256, 512\}$), enabling a consistent comparison across scales of representation.

Training was performed for 200 epochs using the AdamW optimizer with a learning rate of 10^{-3} and a batch size of 100. All experiments used fixed random seeds and stratified splits to ensure reproducibility. Evaluation was based on a comprehensive set of quantitative metrics: reconstruction quality via per-pixel mean squared error (MSE), generative quality via the evidence lower bound (ELBO), latent linear separability using a logistic regression probe, calibration performance through negative log-likelihood (NLL), Brier score, and expected calibration error (ECE), as well as unsupervised clustering measures using normalized mutual information (NMI) and adjusted Rand index (ARI).

Each model is trained for 200 epochs using the AdamW optimizer with a learning rate of 10^{-3} and a batch size of 100. Datasets include the Laroche MNIST variants (*basic*, *rotated*, *background images*, *background random*), Fashion-MNIST, CIFAR-10, and CIFAR-100. For each dataset, both VAE and MVAE models are trained with latent sizes $\{2, 4, 16, 32, 256, 512\}$ depending on input dimensionality.

All models employ a symmetric fully connected architecture with one hidden layer of 500 units in both encoder and decoder. The VAE models use diagonal-covariance posteriors,

whereas the MVAE models incorporate a global coupling matrix as described in Section IV.

B. Quantitative Evaluation

a) *Larochelle MNIST Variants*.: Across rotated, background-images, and background-random settings, MVAE consistently strengthens calibration (NLL/Brier/ECE \downarrow) with comparable or better reconstruction (MSE \downarrow) and structure (NMI/ARI \uparrow). On **MNIST Rotated** (Table V), MVAE shows clear gains at mid latent sizes (e.g., $z=4, 16$) in probe accuracy and calibration, while very large z yields small trade-offs (VAE edges on accuracy/NLL, MVAE on ECE). On **MNIST Background Images** (Table VI), results are near-ties with repeated MVAE calibration wins and negligible MSE deltas; atypical low-accuracy rows behave similarly for both models. On the noisier **MNIST Background Random** (Table VII), MVAE is consistently strong across z , improving probe accuracy, NLL/Brier, ECE, and often NMI/ARI.

b) *Fashion-MNIST*.: As shown in Table III, MVAE is competitive or better at nearly all z . Reconstruction is matched or slightly improved, while calibration metrics frequently favor MVAE (e.g., at $z=4$ and $z=16$ with NLL/Brier/ECE \downarrow). Linear-probe accuracy and clustering (NMI/ARI) exhibit modest but recurring MVAE gains, especially at mid ($z=4-16$) and large ($z=512$) latent sizes.

c) *CIFAR-10 and CIFAR-100*.: On **CIFAR-10** (Table I), small z shows mixed outcomes (MVAE improves calibration and structure; VAE may edge accuracy at $z=2$). In the mid- z regime (e.g., $z=16$), MVAE improves accuracy and calibration concurrently; at very large z (256–512), accuracy differences are marginal (often a slight VAE edge) while

Latent	MSE/test ↓		Probe Acc. ↑		Probe NLL ↓		Brier ↓		ECE ↓		NMI ↑		ARI ↑	
	VAE	MVAE												
2	0.036	0.035	0.221	0.213	2.174	1.889	0.871	0.870	0.046	0.036	0.073	0.079	0.034	0.037
4	0.029	0.029	0.265	0.259	2.065	2.067	0.842	0.843	0.037	0.030	0.093	0.091	0.050	0.047
16	0.019	0.020	0.326	0.341	1.899	1.889	0.797	0.793	0.030	0.038	0.097	0.106	0.055	0.058
32	0.015	0.015	0.373	0.370	1.800	1.810	0.766	0.769	0.030	0.034	0.109	0.113	0.063	0.061
256	0.015	0.015	0.425	0.419	1.639	1.659	0.714	0.720	0.033	0.030	0.106	0.111	0.057	0.059
512	0.015	0.016	0.430	0.420	1.628	1.679	0.709	0.725	0.026	0.031	0.119	0.117	0.063	0.062

TABLE I: VAE vs MVAE on **Cifar10** across latent sizes. Best per cell is bold.

Latent	MSE/test ↓		Probe Acc. ↑		Probe NLL ↓		Brier ↓		ECE ↓		NMI ↑		ARI ↑	
	VAE	MVAE												
2	0.037	0.037	0.037	0.036	4.423	4.429	0.984	0.985	0.008	0.007	0.174	0.175	0.012	0.012
4	0.029	0.030	0.075	0.077	4.162	4.147	0.973	0.973	0.019	0.020	0.203	0.206	0.018	0.019
16	0.018	0.019	0.137	0.139	3.821	3.821	0.945	0.946	0.020	0.024	0.219	0.217	0.026	0.026
32	0.015	0.016	0.165	0.169	3.667	3.660	0.930	0.930	0.017	0.021	0.225	0.222	0.028	0.027
256	0.016	0.016	0.199	0.202	3.471	3.469	0.908	0.907	0.025	0.023	0.223	0.224	0.027	0.028
512	0.015	0.016	0.198	0.194	3.509	3.505	0.913	0.912	0.031	0.026	0.223	0.225	0.027	0.026

TABLE II: VAE vs MVAE on **Cifar100** across latent sizes. Best per cell is bold.

Latent	MSE/test ↓		Probe Acc. ↑		Probe NLL ↓		Brier ↓		ECE ↓		NMI ↑		ARI ↑	
	VAE	MVAE												
2	0.014	0.015	0.804	0.797	0.542	0.548	0.275	0.280	0.022	0.018	0.558	0.535	0.425	0.379
4	0.015	0.015	0.863	0.865	0.399	0.385	0.201	0.195	0.034	0.026	0.502	0.528	0.365	0.374
16	0.027	0.027	0.640	0.670	1.097	0.959	0.498	0.447	0.102	0.069	0.531	0.544	0.356	0.374
32	0.015	0.014	0.819	0.815	0.510	0.506	0.259	0.257	0.027	0.025	0.527	0.523	0.384	0.377
256	0.019	0.019	0.754	0.724	0.701	0.767	0.350	0.381	0.030	0.024	0.589	0.560	0.450	0.400
512	0.016	0.016	0.863	0.865	0.389	0.381	0.197	0.194	0.026	0.026	0.526	0.541	0.353	0.369

TABLE III: VAE vs MVAE on **Fashion MNIST** across latent sizes. Best per cell is bold.

Latent	MSE/test ↓		Probe Acc. ↑		Probe NLL ↓		Brier ↓		ECE ↓		NMI ↑		ARI ↑	
	VAE	MVAE	VAE	MVAE	VAE	MVAE	VAE	MVAE	VAE	MVAE	VAE	MVAE	VAE	MVAE
2	0.0121	0.0119	0.904	0.910	0.308	0.298	0.141	0.136	0.0147	0.0137	0.623	0.641	0.557	0.579
4	0.0119	0.0120	0.943	0.951	0.192	0.168	0.087	0.076	0.021	0.019	0.598	0.623	0.527	0.552
16	0.0394	0.0398	0.605	0.561	1.145	1.215	0.516	0.554	0.083	0.076	0.525	0.514	0.389	0.376
32	0.0114	0.0111	0.913	0.924	0.287	0.254	0.130	0.115	0.018	0.013	0.589	0.642	0.497	0.582
256	0.0280	0.0277	0.860	0.864	0.572	0.562	0.232	0.227	0.073	0.074	0.571	0.582	0.443	0.456
512	0.0126	0.0128	0.945	0.951	0.187	0.175	0.084	0.078	0.023	0.022	0.572	0.602	0.481	0.528

TABLE IV: VAE vs MVAE on **MNIST Basic** across runs. Best per cell is bold.

MVAE retains ECE/NLL/Brier advantages. On **CIFAR-100** (Table II), MVAE yields small, steady gains across z in accuracy and calibration, with NMI/ARI typically equal or slightly improved.

C. Ablation on Latent Dimensionality

Increasing z improves reconstruction (MSE ↓) until saturation (e.g., CIFAR-10 stabilizes near 0.015–0.016 from $z \geq 32$). Probe accuracy generally rises with z before plateauing or slightly regressing at extreme sizes; clustering follows similar trends. Calibration is non-monotone: MVAE’s NLL/Brier/ECE typically improve from small to mid z and fluctuate mildly at the largest z , reflecting bias–variance trade-offs in predictive

entropy. Overall, MVAE’s advantage is most pronounced at *mid-range* z (MNIST: 4–32; CIFAR: 16–256), where correlated posteriors deliver concurrent gains in calibration, linear separability, and clustering without sacrificing reconstruction; at very large z , both models converge in MSE and metric leadership may swap by dataset, while MVAE’s calibration remains robust.

D. Qualitative Evaluation

a) *Reconstruction fidelity*: Figure 3 (first strip) shows triplets at $d_z=32$ (input, VAE recon, MVAE recon). Both models reconstruct faces sharply, yet MVAE preserves high-contrast facial contours (eye corners, nostrils, lip edges) with

Latent	MSE/test ↓		Probe Acc. ↑		Probe NLL ↓		Brier ↓		ECE ↓		NMI ↑		ARI ↑	
	VAE	MVAE												
2	0.016	0.016	0.486	0.494	1.391	1.387	0.632	0.628	0.021	0.021	0.135	0.143	0.071	0.074
4	0.014	0.014	0.677	0.701	0.989	0.923	0.450	0.421	0.080	0.073	0.125	0.098	0.065	0.052
16	0.049	0.049	0.246	0.197	2.011	2.190	0.804	0.862	0.032	0.050	0.159	0.165	0.061	0.119
32	0.013	0.013	0.525	0.531	1.320	1.305	0.597	0.590	0.022	0.022	0.112	0.122	0.056	0.063
256	0.038	0.038	0.334	0.336	1.693	1.691	0.730	0.730	0.022	0.017	0.175	0.204	0.097	0.111
512	0.014	0.014	0.697	0.685	0.937	0.971	0.427	0.440	0.079	0.064	0.116	0.113	0.060	0.061

TABLE V: VAE vs MVAE on **MNIST Rotated** across latent sizes. Best per cell is bold.

Latent	MSE/test ↓		Probe Acc. ↑		Probe NLL ↓		Brier ↓		ECE ↓		NMI ↑		ARI ↑	
	VAE	MVAE												
2	0.030	0.030	0.668	0.672	1.000	0.989	0.451	0.448	0.029	0.030	0.268	0.215	0.175	0.134
4	0.029	0.029	0.759	0.757	0.755	0.746	0.339	0.336	0.037	0.031	0.235	0.254	0.142	0.156
16	0.046	0.045	0.116	0.116	2.295	2.295	0.898	0.898	0.015	0.012	0.006	0.005	0.002	0.002
32	0.029	0.029	0.711	0.714	0.883	0.879	0.397	0.394	0.025	0.027	0.245	0.231	0.154	0.134
256	0.040	0.040	0.271	0.264	2.083	2.090	0.822	0.823	0.061	0.057	0.082	0.082	0.047	0.049
512	0.031	0.030	0.757	0.749	0.754	0.780	0.339	0.349	0.028	0.028	0.240	0.243	0.154	0.159

TABLE VI: VAE vs MVAE on **MNIST Background Images** across latent sizes. Best per cell is bold.

Latent	MSE/test ↓		Probe Acc. ↑		Probe NLL ↓		Brier ↓		ECE ↓		NMI ↑		ARI ↑	
	VAE	MVAE												
2	0.081	0.081	0.789	0.801	0.649	0.615	0.301	0.286	0.029	0.031	0.436	0.466	0.316	0.340
4	0.081	0.081	0.851	0.853	0.480	0.464	0.222	0.218	0.038	0.035	0.426	0.479	0.303	0.354
16	0.083	0.083	0.545	0.546	1.247	1.234	0.571	0.567	0.075	0.068	0.443	0.430	0.262	0.248
32	0.081	0.081	0.816	0.820	0.576	0.568	0.266	0.261	0.036	0.033	0.433	0.456	0.314	0.346
256	0.081	0.081	0.712	0.703	0.855	0.885	0.397	0.410	0.043	0.044	0.464	0.427	0.311	0.268
512	0.082	0.081	0.851	0.857	0.475	0.454	0.219	0.211	0.031	0.029	0.446	0.470	0.299	0.343

TABLE VII: VAE vs MVAE on **MNIST Background Random** across latent sizes. Best per cell is bold.



Fig. 3: FreyFace reconstructions at $d_z = 32$. Rows show *original* (top), *VAE* (middle), and *MVAE* (bottom). MVAE preserves local structure (nostrils, mouth aperture) and shading more faithfully, reducing over-smoothing. Average pixel MSE: VAE = 4.984×10^{-3} , MVAE = 4.872×10^{-3} (lower is better).

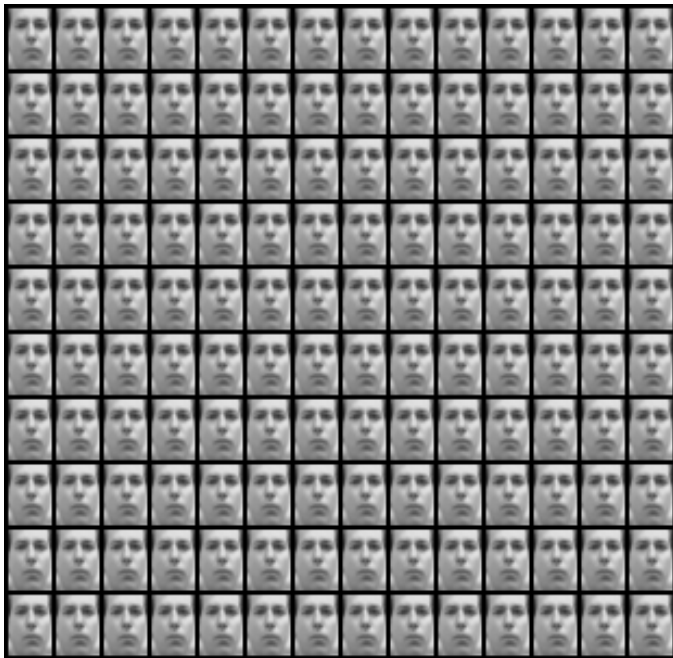
slightly reduced haloing around the cheeks and forehead. This is consistent with a posterior that allocates correlated uncertainty along semantically coherent directions, yielding crisper reconstructions without amplifying noise.

b) Latent-plane sweeps.: We visualize 10×10 traversals along two latent coordinates (z_i, z_j) at $d_z=32$ for MVAE and VAE (Figure 4). Across the grid, both models produce smooth, monotone changes in pose/illumination. MVAE exhibits (i) slightly stronger local contrast (sharper eyelids, nasolabial fold, lip boundary), and (ii) clearer factor transitions (e.g., light direction versus subtle yaw/scale) with fewer degenerate tiles.

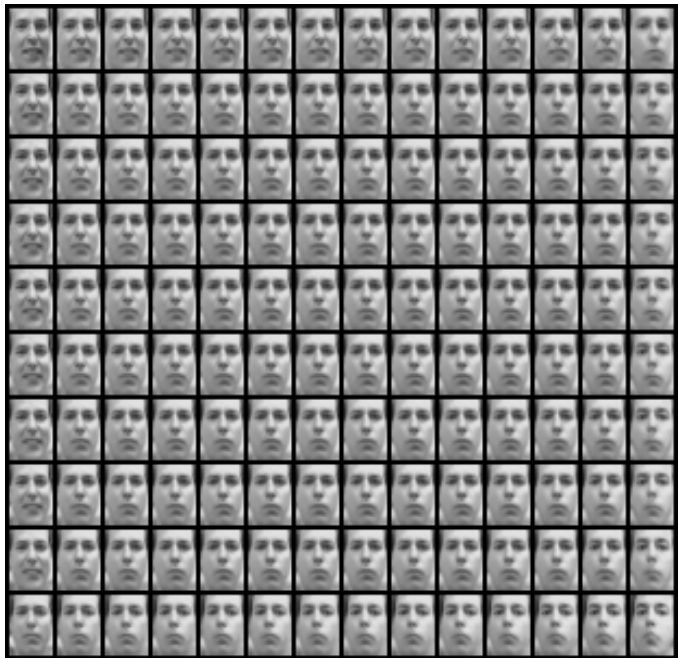
c) Interpretation.: The qualitative patterns align with the quantitative results reported in Section V-B: MVAE’s global coupling plus per-sample scales encourage correlated latent directions that track coherent face factors (lighting, micro-pose, soft tissue shading). This yields slightly sharper reconstructions and smoother, more axis-aligned traversals without sacrificing coverage of the latent plane.

VI. DISCUSSION

MVAE targets a practical gap between diagonal-covariance VAEs and heavier posterior families by injecting *structured*



(a) VAE: sweep over (z_0, z_1) .



(b) MVAE: same sweep.

Fig. 4: Latent-factor sweeps at $d_z = 32$. MVAE exhibits smoother, monotone traversals (pose/expression) with fewer flat regions, indicating better factor geometry due to full-covariance posteriors.

correlations through a single, dataset-wide coupling matrix. Empirically, the approach offers three notable behaviors observed consistently across datasets and latent sizes: (i) calibration improves without sacrificing reconstruction, (ii) linear separability and clustering benefit most in the mid- d_z regime, and (iii) latent-plane traversals become smoother and more axis-aligned, suggesting that correlated uncertainty aligns with semantically coherent factors (e.g., pose, illumination).

From a computational standpoint, the additional parameters in $\mathbf{C} \in \mathbb{R}^{d_z \times d_z}$ scale as $O(d_z^2)$ but are amortized across samples; per-sample costs remain linear in d_z due to the diagonal scales. In practice, this yields training/inference overheads that are modest relative to flow-augmented posteriors while retaining a closed-form KL. The qualitative and quantitative trends are strongest at mid-range latent sizes (MNIST: 4–32; CIFAR: 16–256), where diagonal posteriors underfit cross-dimensional structure and MVAE’s coupling brings the largest calibration and structure benefits. At very high d_z , both models converge in reconstruction and metric leadership may swap by dataset, but MVAE’s calibration typically remains competitive or superior.

VII. CONCLUSION

We introduced MVAE, a Gaussian, closed-form VAE with a full-covariance posterior realized via a global coupling matrix and per-sample scales. The method is simple to implement, analytically tractable, and empirically effective: it improves calibration and unsupervised structure with comparable or better reconstruction across diverse image regimes. Extensive experiments on Larochelle MNIST variants, Fashion-MNIST,

CIFAR-10, and CIFAR-100, together with qualitative sweeps, support the claim that correlated posteriors yield more reliable and useful latent spaces than purely diagonal approximations. To promote reproducibility and future comparisons, we provide complete code, standardized splits/seeds, and metric pipelines.

ACKNOWLEDGMENT

The numerical calculations reported in this paper were fully performed using the EuroHPC Joint Undertaking (EuroHPC JU) supercomputer MareNostrum 5, hosted by the Barcelona Supercomputing Center (BSC). Access to MareNostrum 5 was provided through a national access call coordinated by the Scientific and Technological Research Council of Turkey (TÜBİTAK). We gratefully acknowledge BSC, TÜBİTAK, and the EuroHPC JU for providing access to these resources and supporting this research.

REFERENCES

- [1] D. P. Kingma and M. Welling, “Auto-encoding variational bayes,” in *2nd International Conference on Learning Representations (ICLR)*, 2014.
- [2] D. J. Rezende, S. Mohamed, and D. Wierstra, “Stochastic backpropagation and approximate inference in deep generative models,” in *Proceedings of the 31st International Conference on Machine Learning (ICML)*, 2014, pp. 1278–1286.
- [3] H. Larochelle, D. Erhan, A. Courville, J. Bergstra, and Y. Bengio, “An empirical evaluation of deep architectures on problems with many factors of variation,” in *Proceedings of the 24th International Conference on Machine Learning (ICML)*, 2007, pp. 473–480.
- [4] P. Vincent, H. Larochelle, Y. Bengio, and P.-A. Manzagol, “Extracting and composing robust features with denoising autoencoders,” in *Proceedings of the 25th International Conference on Machine Learning (ICML)*, 2008, pp. 1096–1103.

- [5] H. Xiao, K. Rasul, and R. Vollgraf, "Fashion-mnist: a novel image dataset for benchmarking machine learning algorithms," *arXiv preprint arXiv:1708.07747*, 2017.
- [6] A. Krizhevsky, "Learning multiple layers of features from tiny images," in *Technical Report, University of Toronto*, 2009, technical Report.
- [7] D. J. Rezende and S. Mohamed, "Variational inference with normalizing flows," in *Proceedings of the 32nd International Conference on Machine Learning (ICML)*, 2015, pp. 1530–1538.
- [8] D. P. Kingma, T. Salimans, R. Jozefowicz, X. Chen, I. Sutskever, and M. Welling, "Improving variational inference with inverse autoregressive flow," in *Advances in Neural Information Processing Systems (NeurIPS)*, 2016.
- [9] L. Maaløe, C. K. Sønderby, S. K. Sønderby, and O. Winther, "Auxiliary deep generative models," in *International Conference on Machine Learning (ICML)*, 2016, pp. 1445–1453.
- [10] C. K. Sønderby, T. Raiko, L. Maaløe, S. K. Sønderby, and O. Winther, "Ladder variational autoencoders," in *Advances in Neural Information Processing Systems (NeurIPS)*, 2016, pp. 3738–3746.
- [11] J. M. Tomczak and M. Welling, "Vae with a vampprior," in *International Conference on Artificial Intelligence and Statistics (AISTATS)*, 2018, pp. 1214–1223.
- [12] T. Ryder, A. Golightly, A. S. McGough, and D. Prangle, "Black-box variational inference for stochastic differential equations," in *International Conference on Machine Learning*. PMLR, 2018, pp. 4423–4432.
- [13] X. Wu, E. Dobriban, T. Ren, S. Wu, Z. Li, S. Gunasekar, R. Ward, and Q. Liu, "Implicit regularization and convergence for weight normalization," *Advances in Neural Information Processing Systems*, vol. 33, pp. 2835–2847, 2020.
- [14] I. Higgins, L. Matthey, A. Pal, C. Burgess, X. Glorot, M. Botvinick, S. Mohamed, and A. Lerchner, "beta-vae: Learning basic visual concepts with a constrained variational framework," in *International Conference on Learning Representations (ICLR)*, 2017.
- [15] H. Kim and A. Mnih, "Disentangling by factorising," in *International Conference on Machine Learning (ICML)*, 2018, pp. 2649–2658.
- [16] R. T. Chen, X. Li, R. Grosse, and D. K. Duvenaud, "Isolating sources of disentanglement in variational autoencoders," in *Advances in Neural Information Processing Systems (NeurIPS)*, 2018.
- [17] G. Alain and Y. Bengio, "Understanding intermediate layers using linear classifier probes," in *International Conference on Learning Representations (ICLR Workshop)*, 2017.
- [18] C. Guo, G. Pleiss, Y. Sun, and K. Q. Weinberger, "On calibration of modern neural networks," in *Proceedings of the 34th International Conference on Machine Learning (ICML)*, 2017, pp. 1321–1330.
- [19] G. W. Brier, "Verification of forecasts expressed in terms of probability," *Monthly Weather Review*, vol. 78, no. 1, pp. 1–3, 1950.
- [20] Y. LeCun, L. Bottou, Y. Bengio, and P. Haffner, "Gradient-based learning applied to document recognition," *Proceedings of the IEEE*, vol. 86, no. 11, pp. 2278–2324, 2002.
- [21] M. C. Yavuz and B. Yanikoglu, "Evaluating the efficiency of latent spaces via the coupling-matrix," *arXiv preprint arXiv:2509.06314*, 2025.